Supporting Information

Sulfur Tolerant Subnanometer Fe/Alumina Catalysts for Propane Dehydrogenation

Lohit Sharma,[1] Stephen C. Purdy,[2] Katharine Page,[2,3,4] Srinivas Rangarajan[1] Hien Pham,[5] Abhaya Datye[5] and Jonas Baltrusaitis[1,*]

1. Department of Chemical and Biomolecular Engineering, Lehigh University, 111 Research Drive, Bethlehem, PA 18015, USA
2. Neutron Scattering Division, Oak Ridge National Laboratory, Oak Ridge, TN 37830, USA
3. Shull Wollan Center, Oak Ridge National Laboratory, Oak Ridge, TN 37830, USA
4. Materials Science and Engineering Department, University of Tennessee, Knoxville, TN 37996, USA
5. Center for Microengineered Materials and Department of Chemical & Biological Engineering, University of New Mexico, Albuquerque, NM 87131, USA.

Corresponding Author: Jonas Baltrusaitis: job314@lehigh.edu

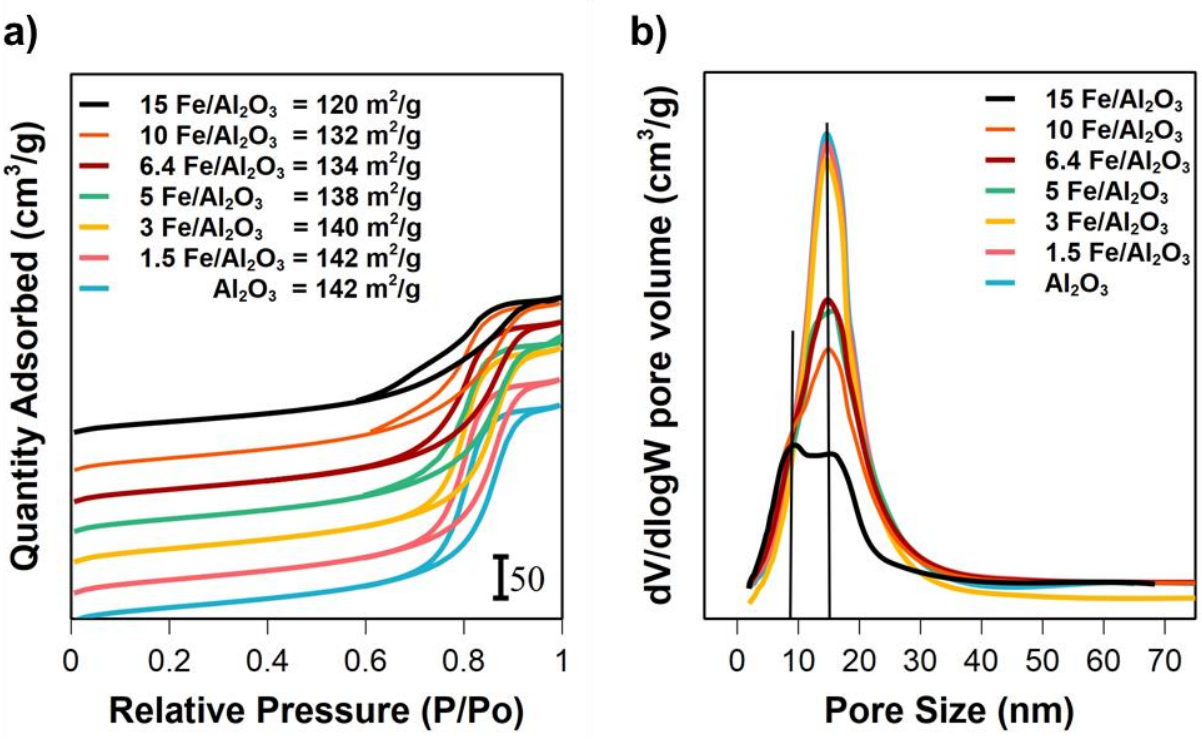

Figure S1. a) Nitrogen physisorption and b) BJH pore size distribution computed from the desorption branch for as-synthesized Fe/Al_2O_3 catalysts.

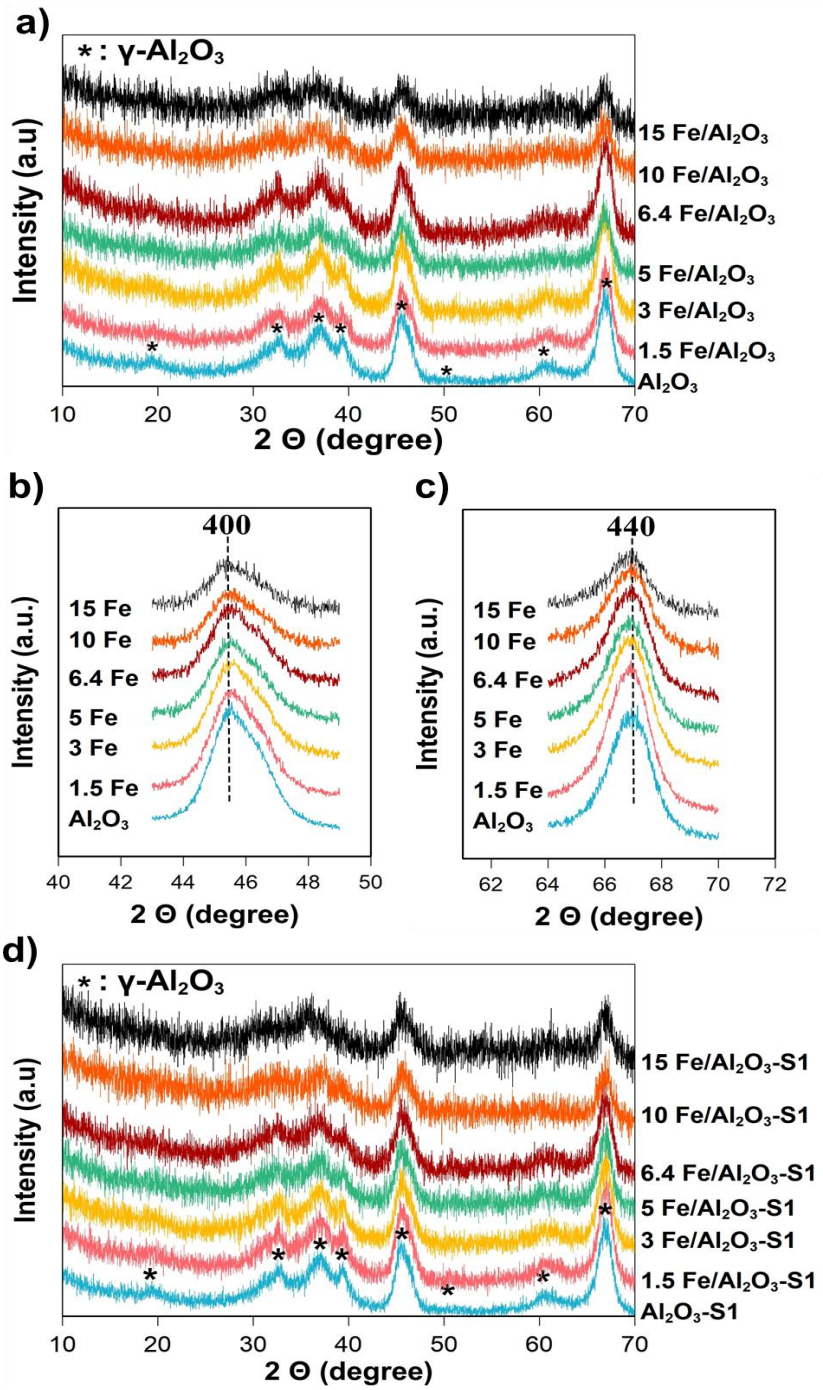

Figure S2. a) *Ex situ* XRD spectra of 0-15 Fe loading (wt.%) over Al_2O_3. Magnified plots of b) 400 and c) 440 planes of as-synthesized catalyst. d) *Ex situ* XRD spectra of as catalyst after 1 PDH cycle for 0-15 Fe/Al_2O_3-S1 with the catalysts pretreated in H_2S before the reaction.

Non Synchrotron XRD. To determine the crystalline identity of the catalysts, pXRD analysis (Empyrean, PANalytical B.V.) was performed. The applied current was 40 mA, and the applied voltage was 45 kV. The diffraction patterns were obtained between 10 and 75°. The radiation source used was Cu $K\alpha_{1,2}$ with Cu $K\alpha_1$ wavelength 1.540598 Å and Cu $K\alpha_2$ wavelength 1.544426 Å. The ratio of $K\alpha_1/K\alpha_2$ was 0.5. The XRD measurements were taken under ambient conditions for all catalysts.

Non synchrotron XRD was used to analyze the phase composition of the as-synthesized and spent catalysts. As shown in **Figure S2a**, Al_2O_3 support displays three typical diffraction peaks at 37.0°, 45.5° and 66.8°, which can be attributed to (311), (400), and (440) planes of γ-Al_2O_3. It was observed that the diffraction peaks related to the Fe_2O_3 crystalline phase were completely absent even for the highest loading of 15% Fe indicating either an amorphous nature or highly dispersed state with no long-range order.[1] The peak intensities of γ-Al_2O_3 became significantly lower with increasing Fe loading. This attenuation of γ-Al_2O_3 peaks could be due to (i) x-ray absorption by Fe-based phase rather than the loss of Al_2O_3 crystallinity,[2] (ii) formation of Fe-alumina solid solution,[3,4] and (iii) formation of intermediates such as $Fe_2O_3.Al_2O_3$.[5] To avoid this synchrotron, XRD was used to attain high resolution data in **Figure 2**. The high flux and photon energy from the synchrotron was necessary to distinguish between the above possibilities.

Data was collected with a slower scan rate (~ 1° per minute) for the (400) and (440) diffraction peaks to observe any peak shift due to Fe incorporated in the γ-Al_2O_3 lattice. As shown **in Figure S2b and S2c**, there was no systematic shift in diffraction peaks of the γ-Al_2O_3 lattice, indicating that Fe^{3+} ions are not substituting Al^{3+} of γ-Al_2O_3.[6] This result is consistent with our synchrotron XRD study (**Figure 2)**. A previous study, also indicated that the iron oxide diffusion into Al_2O_3 occurs above 620 ^oC.[7] In **Figure S2d**, the Fe/Al_2O_3-S1 catalysts do not exhibit peaks either for the iron oxide or iron sulfide phase. These results indicate that the catalysts do not possess either Fe_2O_3/FeS_x crystals with a size greater than 3nm.

TEM, STEM, and EDS.

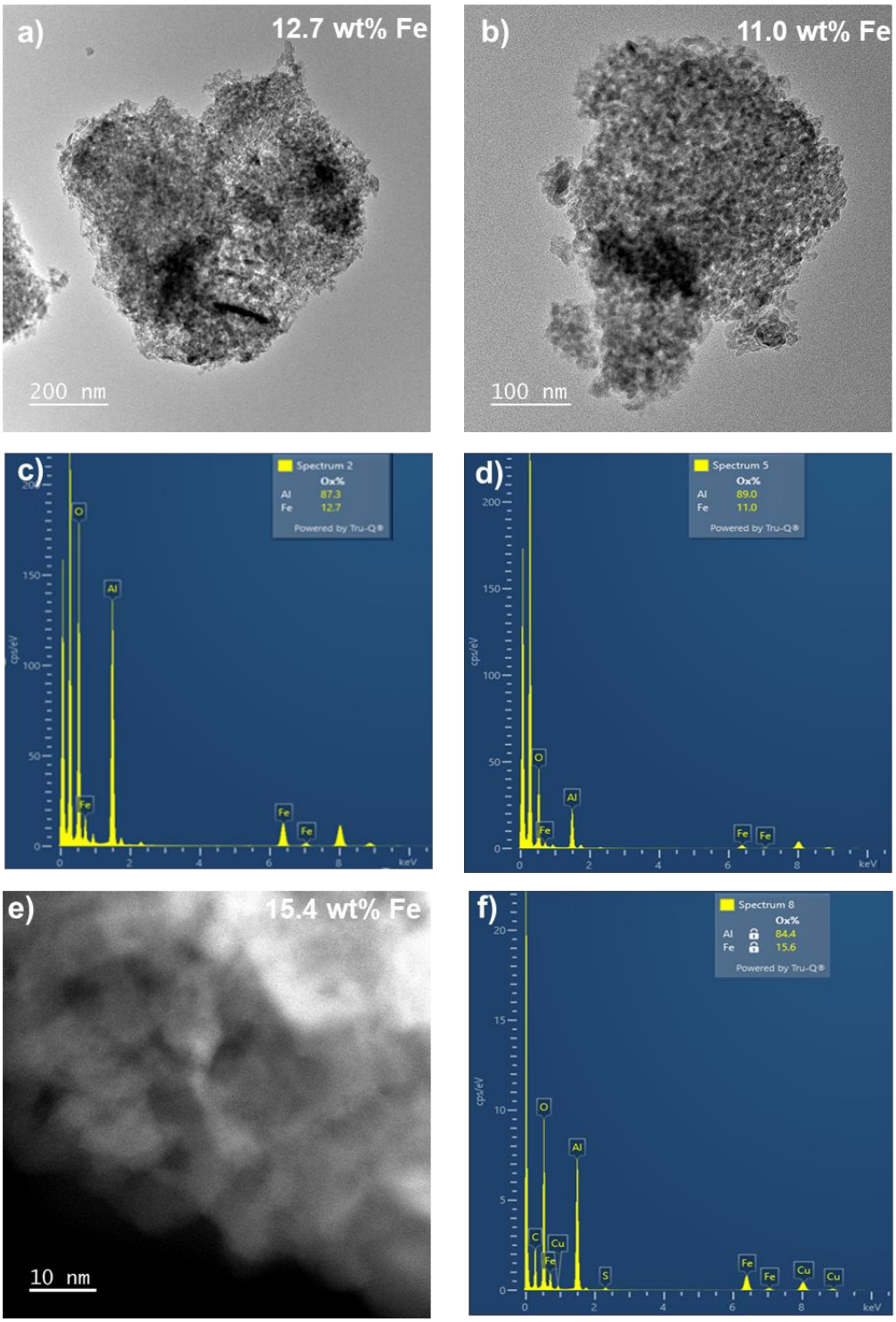

Figure S3. (a) – (b) Low magnification TEM images of the as-synthesized 15 Fe/Al_2O_3 sample, with corresponding EDS data (c) - (d) and higher magnification STEM ADF image (e) along with the EDS data (f). There is no evidence of any crystalline Fe phase despite the high Fe loading.

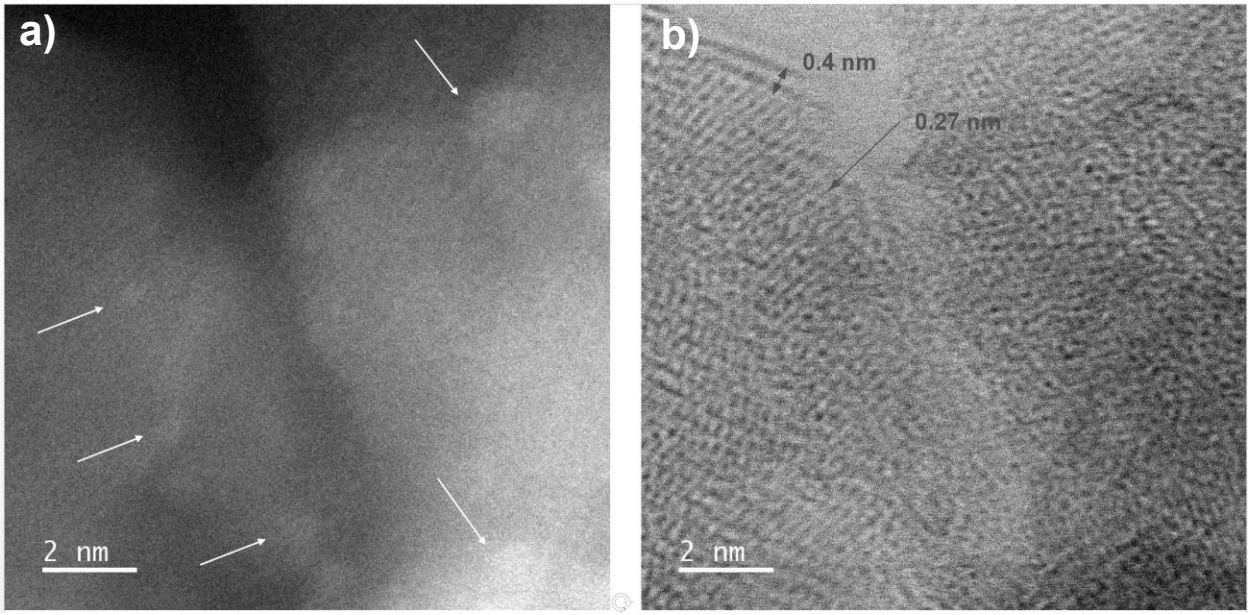

Figure S4. ADF image on the left and ABF image on the right, of the same region of 15 Fe/Al_2O_3 in this oxide form. There are regions of higher contrast in ADF suggesting (arrowed) the presence of Fe containing nanoparticles. But there are no corresponding lattice fringes from these regions, on the right. They appear to blend into the alumina structure. The 0.27 nm alumina fringe corresponding to (220) is identical to the Fe_2O_3 (104) fringe. This suggests there is a layer of iron oxide on the surface, epitaxial with the alumina, as suggested by the PDF analysis. Also, the 0.4 nm surface layer is not consistent with any known alumina reflections, but is close to Fe_2O_3 (012), suggesting an over layer of iron oxide on the alumina.

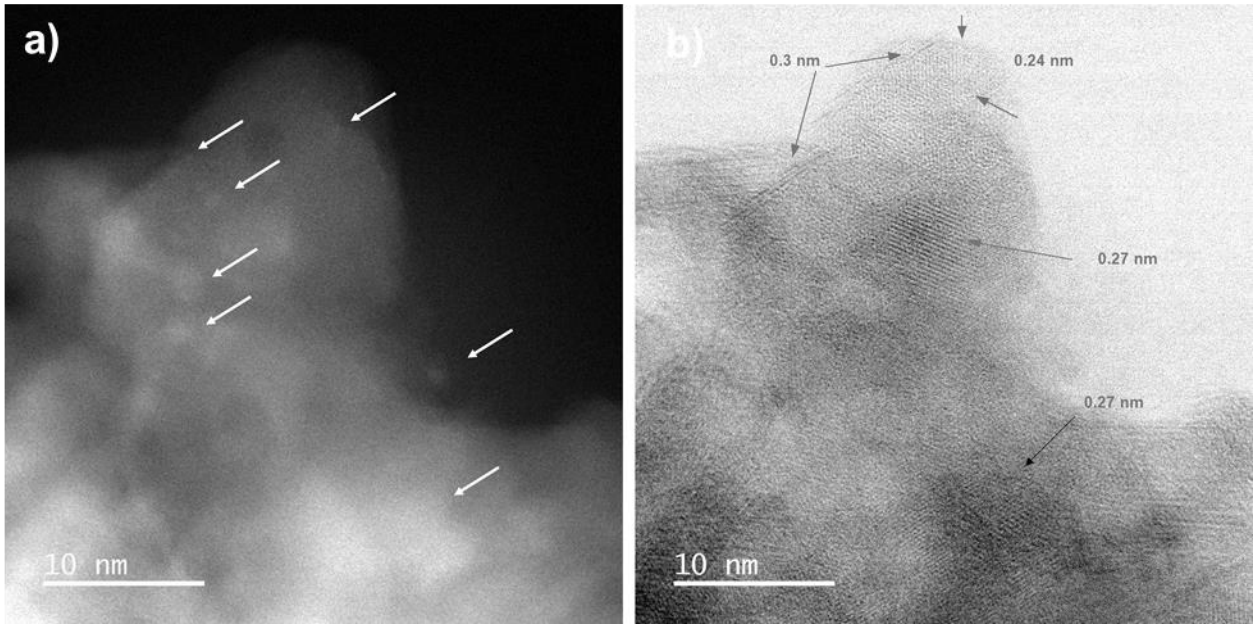

Figure S5. STEM ADF image on the left and the same region of the 15 Fe/Al_2O_3 sample in its oxide form, imaged using STEM ABF on the right. The arrows point to regions of high contrast which would correspond to the presence of Fe, but the corresponding regions on the right show no lattice fringes corresponding to Fe_2O_3. Instead, the fringes all correspond to alumina (311) – 0.24 nm and alumina (220) – 0.27 nm. This would suggest the Fe is present epitaxial on the alumina, because the 0.27 nm fringe also agrees with the Fe_2O_3 (104) reflection. In addition to the nanophase regions, the arrow on the right shows a 0.3 nm lattice fringe on the surface, and the ADF image also shows a possible higher contrast on this surface layer. The 0.3 nm fringe does not correspond to alumina or Fe_2O_3 and might suggest a surface layer of iron oxide on the alumina.

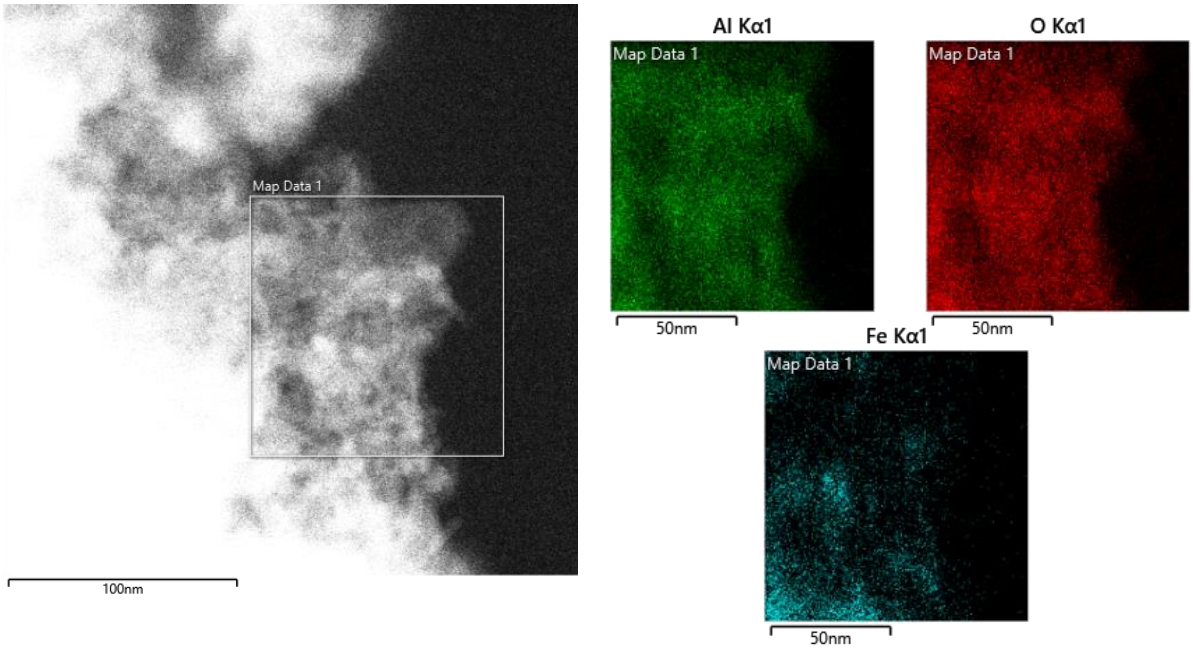

Figure S6. EDS elemental maps of the 15 Fe/Al_2O_3 sample in its oxide form. The maps for Al, O and Fe, come from the region shown in the STEM image (Map Data 1). Iron is dispersed on the alumina. The brighter regions in the electron image and the higher concentration of Fe suggests the presence of nanoparticles, likely due to the high loading. However, as shown in Figures S2 – S3, these high contrast regions do not show any lattice fringes corresponding to iron oxides. Hence, these might be poorly crystallized, or even present as a conformal layer on the alumina since the only lattice fringes seen correspond to alumina.

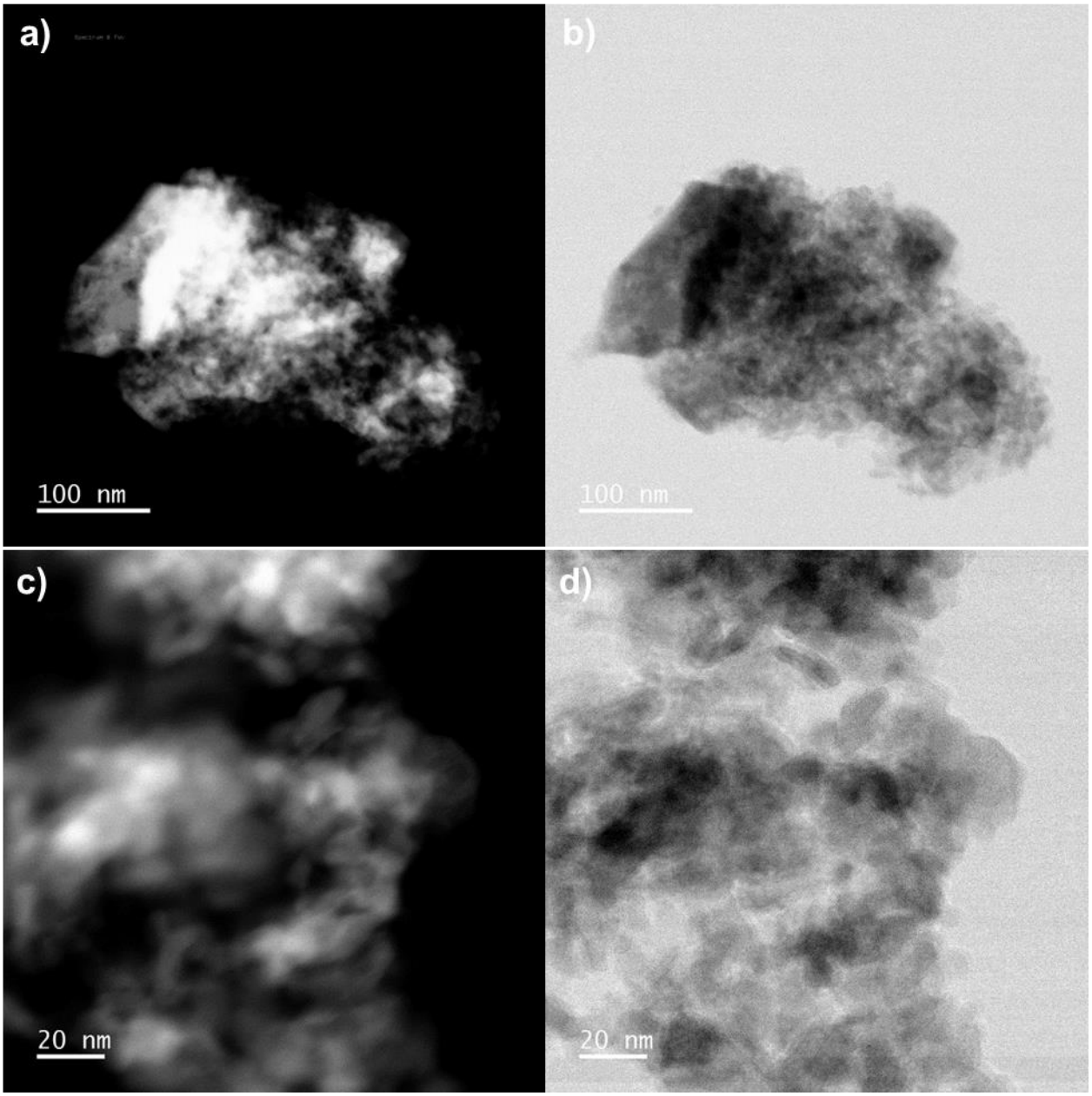

Figure S7. (a) and (c) ADF images of 15 Fe/Al_2O_3-S after sulfiding and (b) and (d) ABF images of the same region. No crystalline phases are seen in this sample, other than alumina.

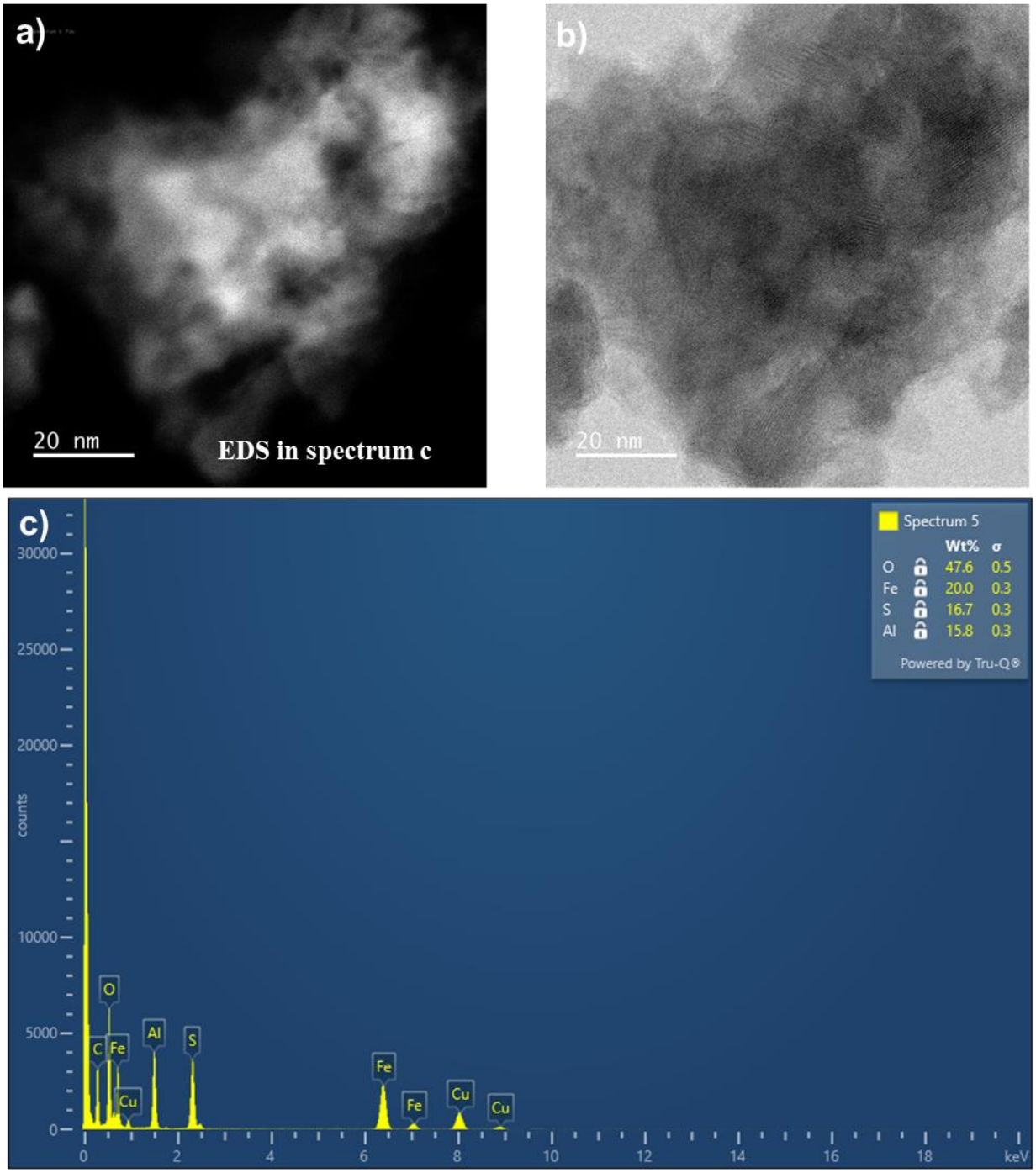

Figure S8. ADF (top left) and ABF (top right) images from the 15 Fe/Al_2O_3-S sample. The EDS spectrum shows that there is a high loading of Fe and S on this sample. However, no crystalline phases are detected (other than alumina) in any of the images.

Figure S9. EDS spectrum of the region analyzed in the map for 6.4 Fe/Al_2O_3-S1 shown in **Figure 3**. The average composition of this sample derived from multiple regions analyzed via EDS analysis was 3.6 wt% Fe and 1.9 wt% S.

Synchrotron PDF.

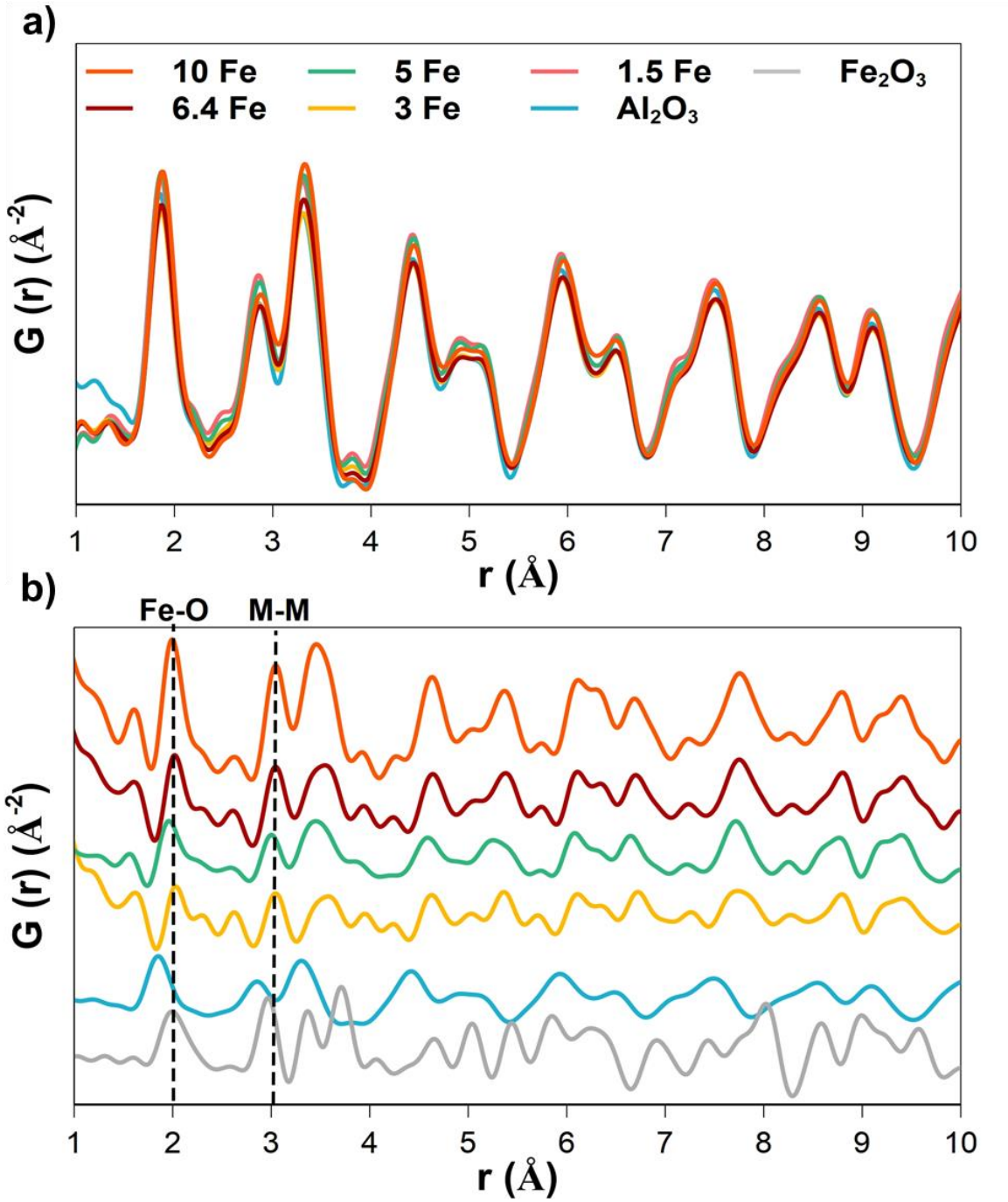

Figure S10. a) Scaled X-ray PDF patterns of Fe/Al_2O_3 catalysts and the bare Al_2O_3 support. b) Difference PDF of Fe/Al_2O_3 catalysts plotted with the PDF of bulk γ-Al_2O_3 and calculated PDF of α-Fe_2O_3.

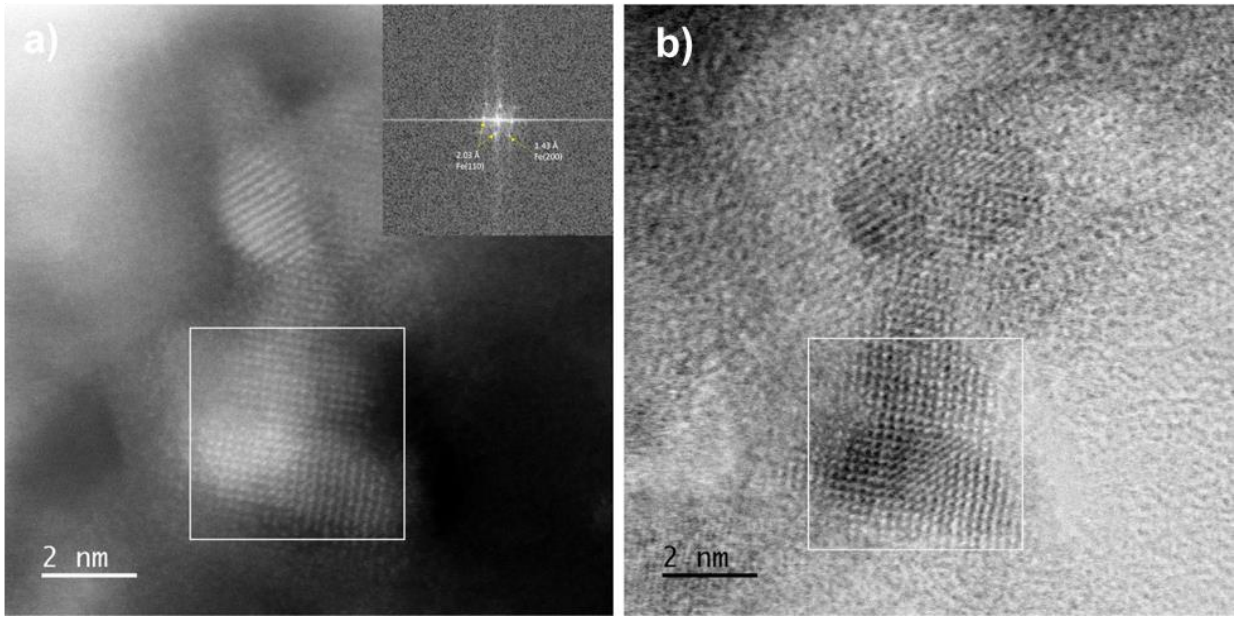

Figure S11. (a) ADF image and (b) ABF image of a metallic Fe nanoparticle in the 6.4 Fe/Al_2O_3-S1 catalyst after one cycle of PDH. This was the only crystalline particle found after recording images of 50 regions from this sample. It demonstrates that Fe is reduced in this sample and since it is passivated by S, it can survive intact even after air exposure. The image is included to show that the microscope has the resolution to detect such nanoparticles if present. They were simply not visible anywhere else in the sample.

XANES and EXAFS.

Table S1. XANES edge energies and pre-edge peak positions for Fe_2O_3 reference and Fe/Al_2O_3 catalysts.

Catalyst	**Pre-edge maximum (eV)**	**XANES edge energy (eV)**
Fe_2O_3	7113.7	7121.8
1.5 Fe/Al_2O_3	7113.2	7121.5
3 Fe/Al_2O_3	7113.2	7121.7
5 Fe/Al_2O_3	7113.1	7121.5
6.4 Fe/Al_2O_3	7113.1	7121.5
10 Fe/Al_2O_3	7113.2	7121.5

Table S2. Fitted Coordination Numbers, Interatomic Distances, Debye-Waller Factors, Energy Shift Parameters, and R-Factor Values for Fits to Fourier-transformed Fe K-Edge EXAFS of Fe/Al_2O_3 catalysts. The fits are provided in the SI (**Figure S12-S20**).

Catalyst	**Path**	**CN**	**E_0 (eV)**	**R (Å)**	**ε**	**σ^2 (Å^2/10^{-3})**	**R factor**
1.5 Fe/Al_2O_3	Fe-O	3.9±0.5	1.4±0.9	1.937±0.009	0.003± 0.005	5.5±2	0.0026
	Fe-O	1.1±0.4		2.11±0.01			
	Fe-Al	0.7±0.5		2.89±0.01		1.9±7	
	Fe-Al	1.2±0.8		3.36±0.02			
3 Fe/Al_2O_3	Fe-O	3.9±0.4	1±1.1	1.94±0.009	0.002± 0.005	5.9±2	0.0045
	Fe-O	0.9±0.5		2.11±0.01			
	Fe-Al	0.9±0.9		2.89±0.01		9±9	
	Fe-Al	2.3±1.4		3.36±0.02			
5 Fe/Al_2O_3	Fe-O	3.5±0.5	1±1.1	1.92±0.01	0.001± 0.006	5±2	0.0054
	Fe-O	1.2±0.4		2.09±0.01			
	Fe-Al	0.6±0.5		2.87±0.02		0±7	
	Fe-Al	1.2±0.8		3.33±0.02			
6.4 Fe/Al_2O_3	Fe-O	3.3±0.4	1.6±1.1	1.93±0.01	0.009± 0.006	4.3±2	0.0056
	Fe-O	1.3±0.3		2.09±0.01			
	Fe-Al	0.8±0.6		2.87±0.02		2±7	
	Fe-Al	1.4±0.9		3.33±0.02			
10 Fe/Al_2O_3	Fe-O	3.9±0.6	2.3±1.3	1.93±0.01	0.022± 0.007	7±7	0.0071
	Fe-O	1.6±0.6		2.11±0.01			
	Fe-Al	0.9±0.9		3.03±0.02		7±6	
	Fe-Al	2.3±1.4		3.56±0.02			

Before multi-shell models were fit, two different models of the Fe-O coordination environment were tested: having either a single Fe-O bond distance, or two Fe-O bond distances (as in Fe_2O_3). Fitting results of these models are given in the supplemental information. The R-factor and reduced chi-squared value of the 2-path fit reduced relative to that of the 1-path fit, supporting a structure with multiple Fe-O bond distances. While the Fe-O peak looks much more symmetric than bulk Fe_2O_3, it has a shoulder at 2 Å which is better fit when the 2nd long Fe-O path is included in the model.

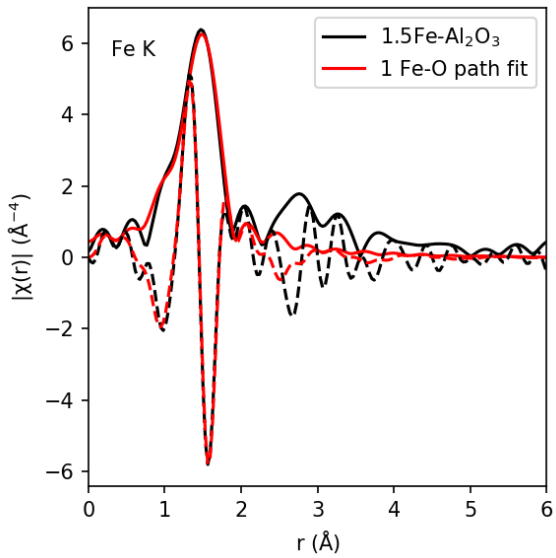

Figure S12: k^3 weighted EXAFS magnitude (solid) and imaginary (dashed) components of 1.5 Fe/Al_2O_3 with data in black and single Fe-O path fit in red.

Table S3: EXAFS fit parameters for single Fe-O path first shell fit of 1.5 Fe/Al_2O_3

1.5 Fe/Al_2O_3 EXAFS fit Δk = 2.7-11 Å^{-1}, ΔR = 1.0-2.3 Å (r factor=0.0072, χ^2_{red}= 87.4)					
Path	CN	R_{eff} (Å)	ΔR (Å)	σ^2 (Å^2/10^{-3})	E_0 (eV)
Fe-O	4.7±0.4	1.9437	0.004±0.01	8±2	-0.1±1.0

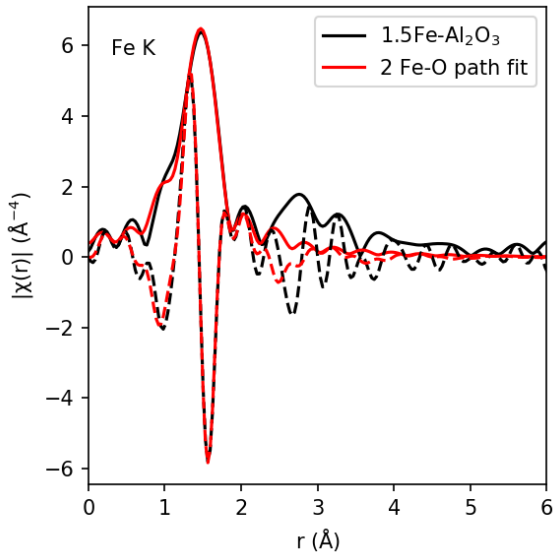

Figure S13. k^3 weighted EXAFS magnitude (solid) and imaginary (dashed) components of 1.5 Fe/Al_2O_3 with data in black and 2 Fe-O path fit in red.

Table S4: EXAFS fit parameters for two Fe-O path first shell fit of 1.5 Fe/Al_2O_3

1.5 Fe/Al_2O_3 EXAFS fit Δk = 2.7-11 $Å^{-1}$, ΔR = 1.0-2.3 Å (r factor=0.00345, χ^2_{red}= 61.0)					
Path	CN	R_{eff} (Å)	ΔR (Å)	σ^2 ($Å^2/10^{-3}$)	E0 (eV)
Fe-O	3.7±0.6	1.9437	0.01±0.01	4±3	1.2±1.0
Fe-O	1.1±0.5	2.1144	0.01±0.01	4±3	1.2±1.0

To identify the 2nd nearest neighbor in the Fe/Al_2O_3 catalysts, EXAFS data of 1.5 Fe/Al_2O_3 and Fe_2O_3 were compared in R space and Q space. While the 2nd shell scattering magnitude of the Fe/Al_2O_3 catalyst aligns with that of Fe-Fe scattering in Fe_2O_3, the imaginary component of the peak is quite different in shape, suggesting a neighbor other than Fe. Further evidence of this can be seen in the real component of the Q space back-transform of the 2nd shell between 2.3-3.0 Å for the 1.5 Fe/Al_2O_3 and 2.1-2.9 Å for Fe_2O_3. Lighter scatterers have their highest q (or k) space magnitude at lower wavenumber and the oscillations decay faster at high q (or k) compared to a heavier scatterer. From the q space plot below, the 2nd shell peak from 1.5 Fe/Al_2O_3 has a maximum around 4.5 $Å^{-1}$ whereas the 2nd shell peak in Fe_2O_3 peaks at 6.5 $Å^{-1}$. This is consistent with Fe in the catalyst having a light 2nd nearest neighbor such as Al.

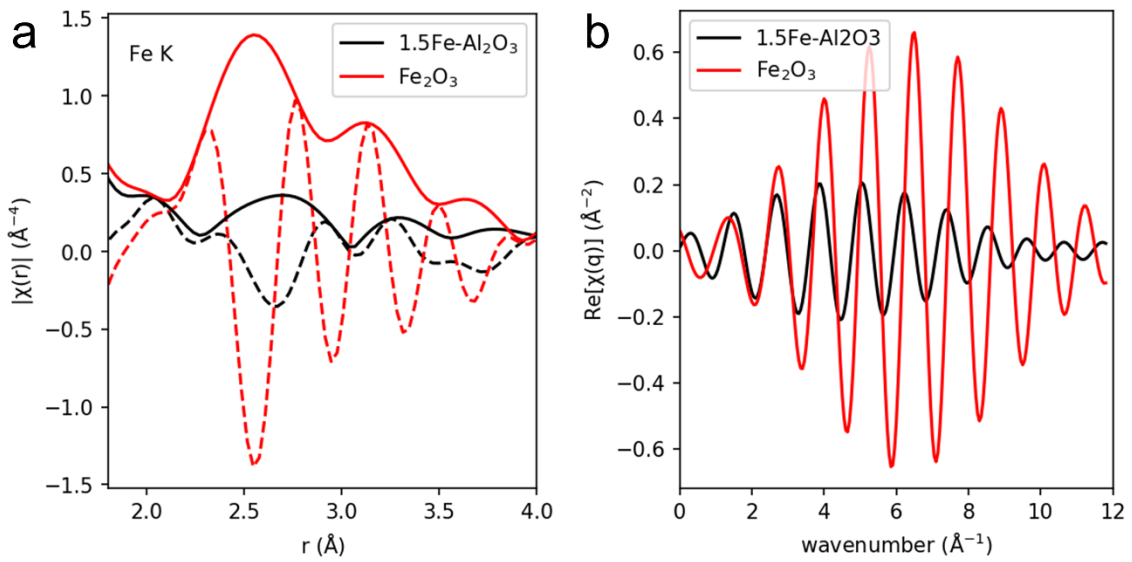

Figure S14. a) Expanded view of k^3 weighted EXAFS 2nd shell scattering magnitude (solid line) and imaginary components (dashed line) for 1.5 Fe/Al_2O_3 (black) and Fe_2O_3 (red). b) Q space real component of 2nd shell scattering for 1.5 Fe/Al_2O_3 from 2.3-3.0 Å (black) and Fe_2O_3 from 2.1-2.9 Å (red).

EXAFS Fitting

Table S5. EXAFS fit parameters for iron foil

Fe Foil EXAFS fit Δk = 2.75-13.5 $Å^{-1}$, ΔR = 1.0-2.9 Å (r factor=0.0058, χ^2_{red}= 1887.9)						
Path	CN	$S0^2$	E_0 (eV)	R (Å)	ε	σ^2 ($Å^2/10^{-3}$)
Fe-Fe	=8	0.738±0.06	5.8±1.2	2.466±0.006	-0.008±0.003	4.8±0.6
Fe-Fe	=6	0.738±0.06	5.8±1.2	2.848±0.007		6±1

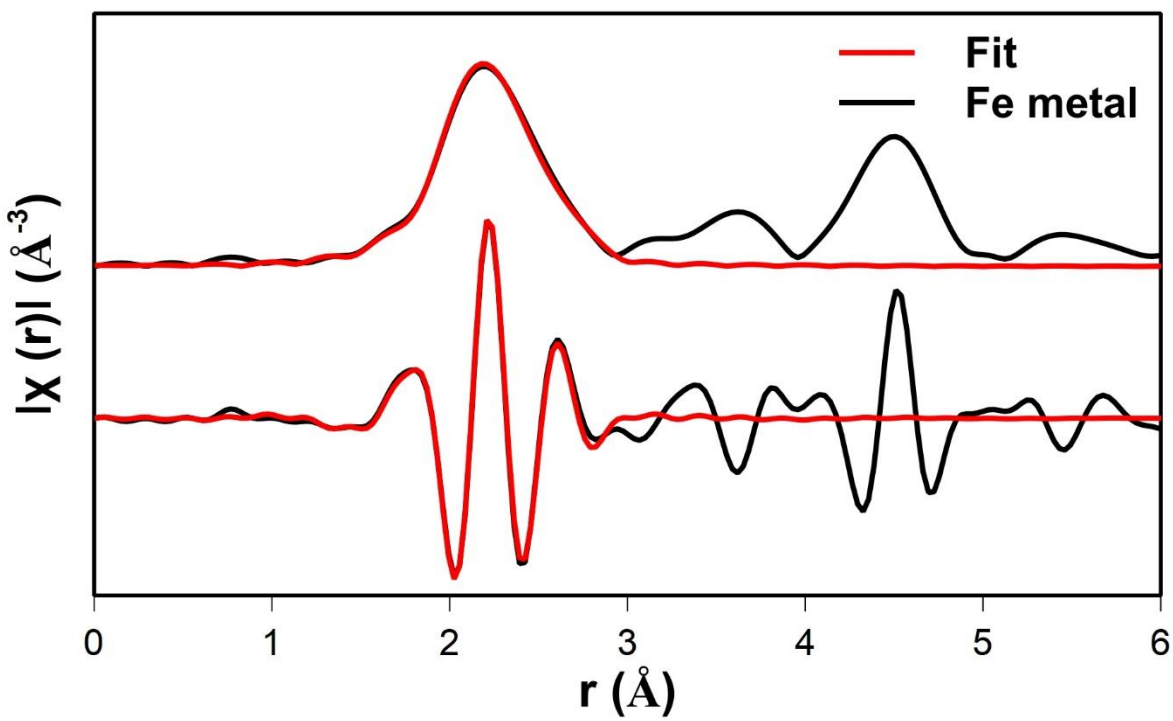

Figure S15. R-space EXAFS spectra and fit of iron foil.

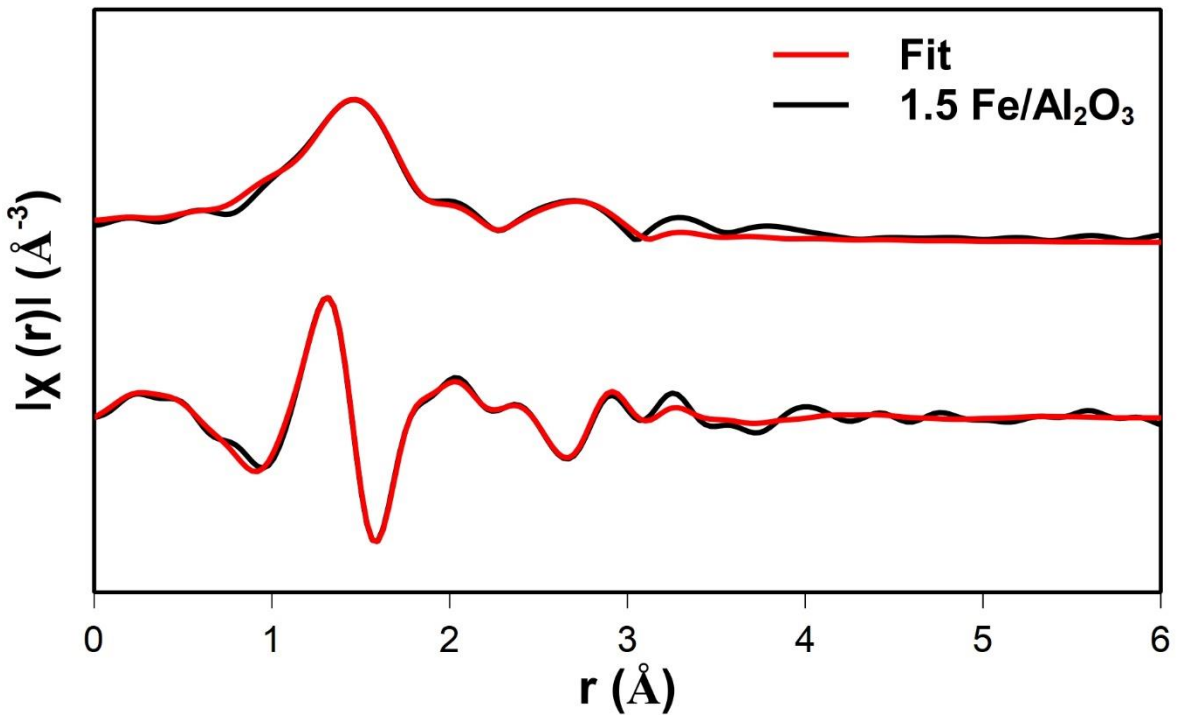

Figure S16. R-space EXAFS spectra and fit of 1.5 Fe/Al_2O_3.

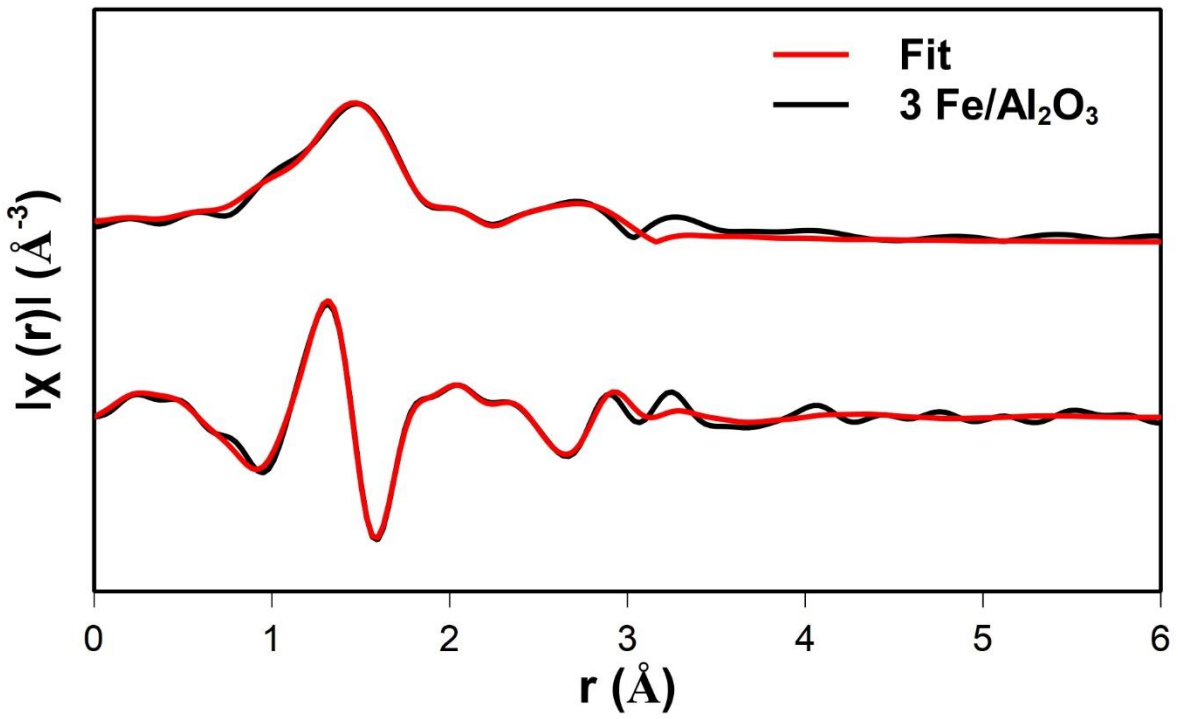

Figure S17. R-space EXAFS spectra and fit of 3 Fe/Al_2O_3.

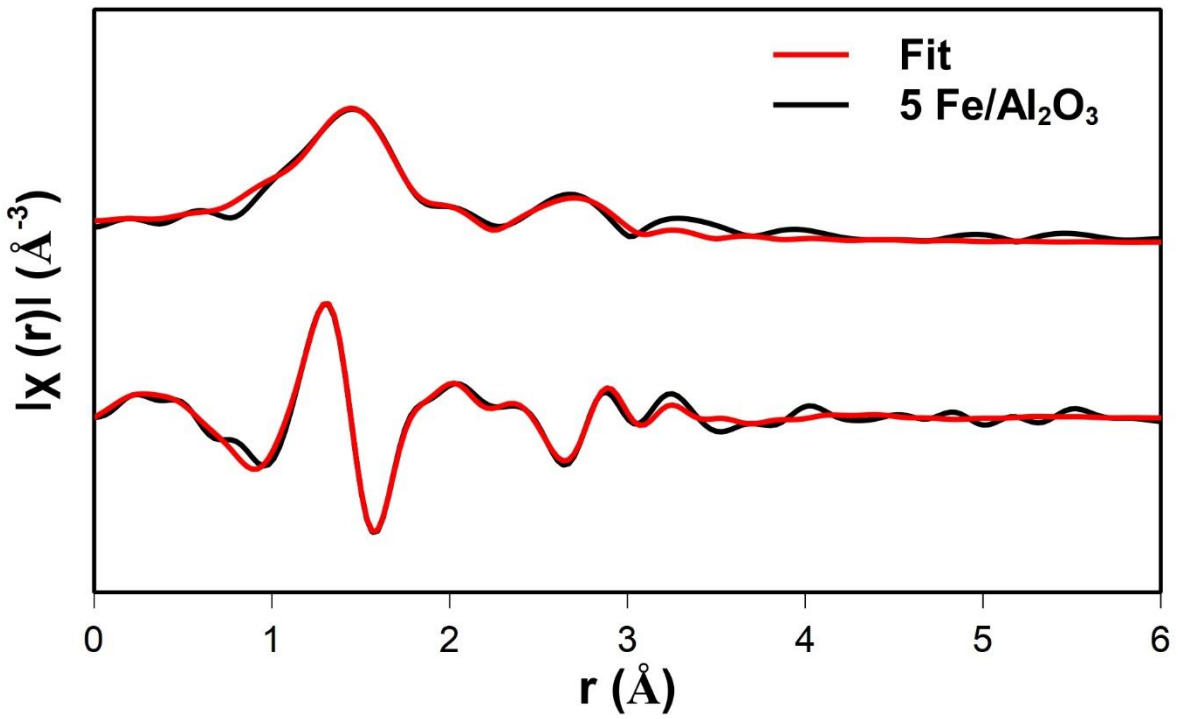

Figure S18. R-space EXAFS spectra and fit of 5 Fe/Al_2O_3.

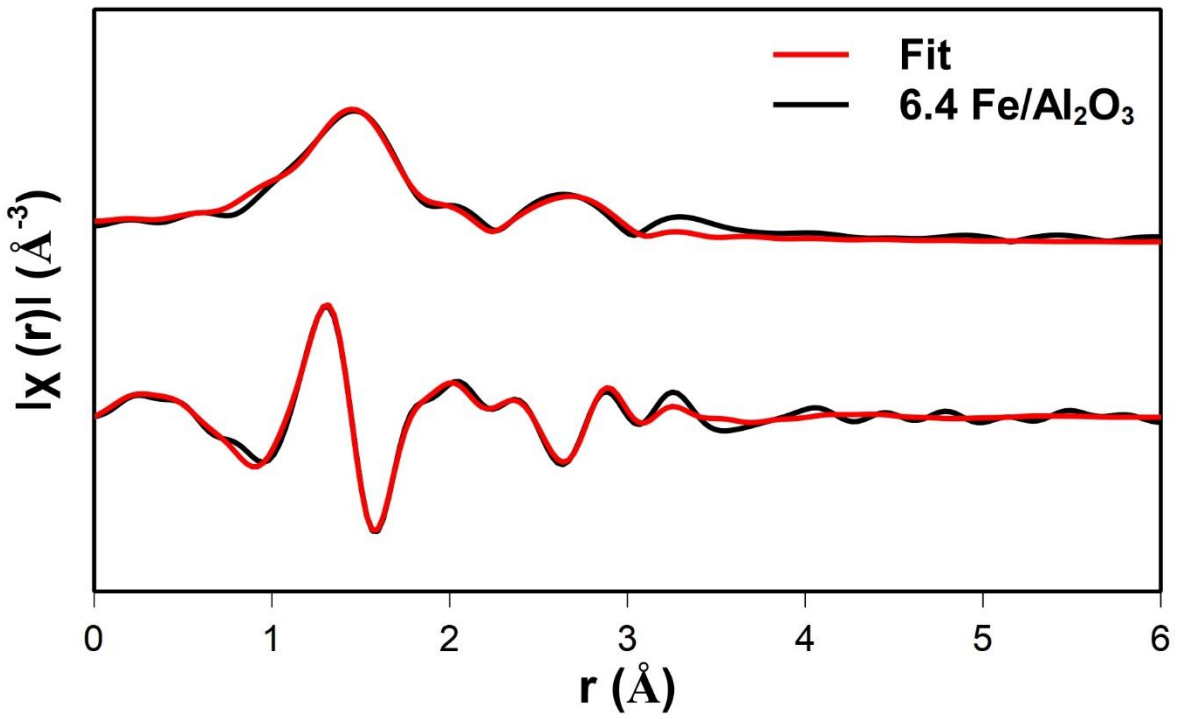

Figure S19. R-space EXAFS spectra and fit of 6.4 Fe/Al_2O_3

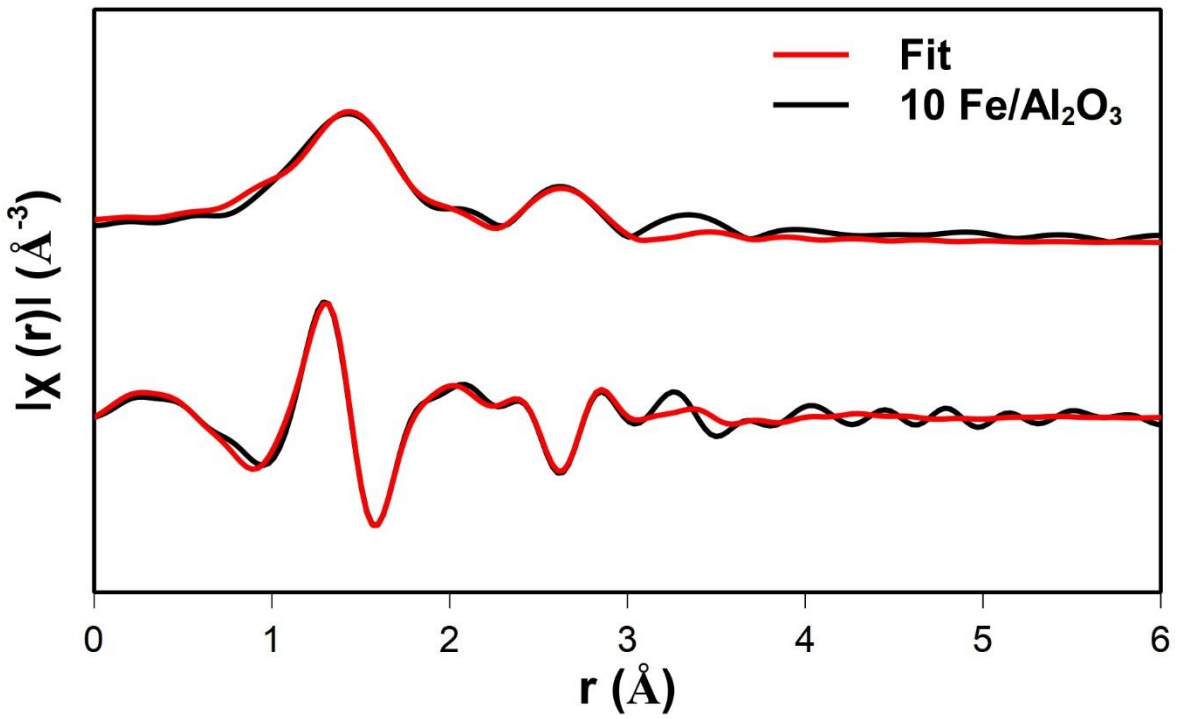

Figure S20. R-space EXAFS spectra and fit of 10 Fe/Al_2O_3.

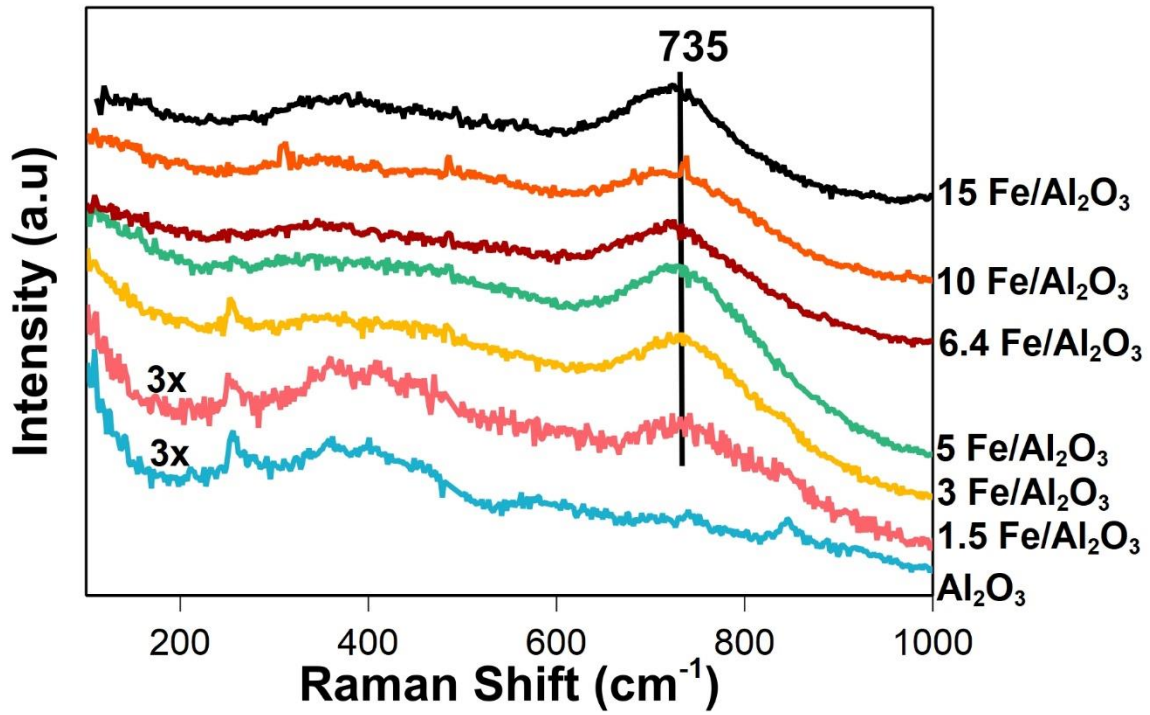

Figure S21. Raman spectra of Fe/Al_2O_3 as-synthesized catalysts after air calcination.

Experimental Method for Raman Spectroscopy. *Ex situ* Raman spectra were acquired using a WITec alpha3000 R confocal Raman microscope using a 532 nm laser and x100 objective.

Wachs *et al*.[8,9] assigned ~750 cm^{-1} peak to surface Fe^{3+} ion. Clearly, the bands associated with Fe_2O_3 peaks below 400 cm^{-1} were not present in the samples. [10,11] The broad bands at 735 cm^{-1} does not match other iron phases such as α-FeOOH (550, 474, 414, 397, 298 cm^{-1}), γ-FeOOH (380, 252 cm^{-1}), Fe0 (663, 616 cm^{-1}) or Fe_3O_4 (663, 616 cm^{-1}).[8,9]

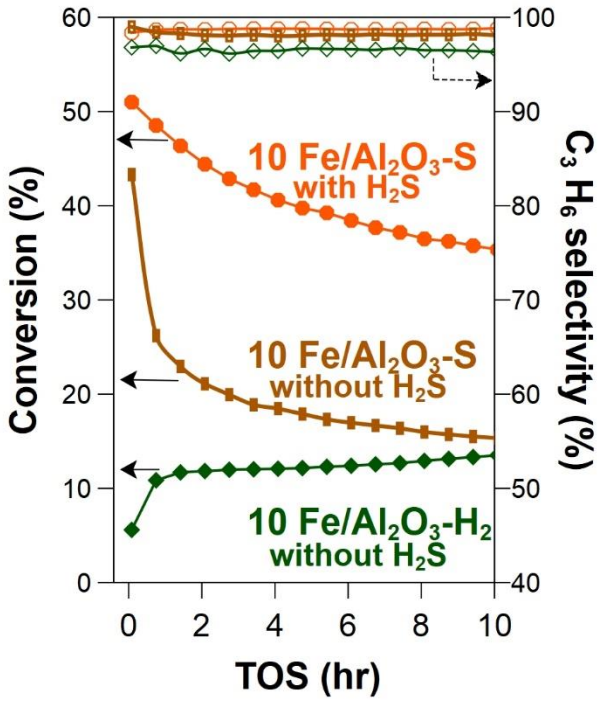

Figure S22. C_3H_8 conversion and C_3H_6 selectivity for different pretreatments for 10 Fe/Al_2O_3. The feed contained 1.1% C_3H_8, 1% H_2, with (0.1%) and without H_2S co-feed, and the reaction temperature was 560 °C. The 10 Fe/Al_2O_3-H_2 catalyst was pretreated in 1% H_2 at 600 °C for 4 hours. The 10 Fe/Al_2O_3-S catalyst was pretreated in 1% H_2S at 600 °C for 4 hours. The total volumetric flow rate was 50 ml/min and 200 mg of catalyst was used. Solid diamonds, rectangles, and octagon represent conversion, while empty diamonds, rectangles, and octagon represent C_3H_6 selectivity. This figure reports the conversion with TOS of **Figure 7a**.

Table S6. Tabulated steady-state reactivity properties of the Fe supported catalysts with different Fe (wt.%) loading under different H_2S pretreatment and co-feed. Reaction conditions were as follows: T=560 °C, C_3H_8=1.1%, H_2=1%, and H_2S =0.1% (if present) and 200 mg of catalyst was used. The total volumetric flow rate was 50 ml/min. This table reports the high conversion data.

Co-feed	**Catalyst**	**S_i (%)**	**$rate_i$** (moles g^{-1} s^{-1}) [**X_i** (%)]	**S_f (%)**	**$rate_f$** (moles g^{-1} s^{-1}) [**X_f** (%)]	**F/I**
$H_2 + H_2S$	Al_2O_3-S	93.4	3.30×10^{-7} [15.9]	93.2	2.45×10^{-7} [11.6]	0.73
$H_2 + H_2S$	1.5 Fe/Al_2O_3-S	98.5	6.59×10^{-7} [33]	98.7	4.95×10^{-7} [24.8]	0.74
$H_2 + H_2S$	3 Fe/Al_2O_3-S	97.8	7.49×10^{-7} [36.6]	98.7	5.25×10^{-7} [25.8]	0.71
$H_2 + H_2S$	5 Fe/Al_2O_3-S	98.7	9.84×10^{-7} [48]	99.1	7.1×10^{-7} [30]	0.72
$H_2 + H_2S$	6.4 Fe/Al_2O_3-S	98.5	10.7×10^{-7} [51.8]	99.2	7×10^{-7} [34]	0.65
$H_2 + H_2S$	10 Fe/Al_2O_3-S	98.5	9.83×10^{-7} [51]	98.8	6.6×10^{-7} [34.1]	0.67
$H_2 + H_2S$	15 Fe/Al_2O_3-S	98.6	9.92×10^{-7} [47]	98.9	6.7×10^{-7} [30]	0.66
H_2	10 Fe/Al_2O_3-H_2	98.4	1.1×10^{-7} [5.6]	96.1	2.69×10^{-7} [13.5]	2.44
H_2	10 Fe/Al_2O_3-S	98.9	9.13×10^{-7} [43.3]	98.2	3.21×10^{-7} [15.3]	0.35
H_2S	FeS	~65#	~2.7×10^{-9}#	~65#	~2.75×10^{-9}#	---
H_2	SiO_2	~60#	~2.9×10^{-9}#	---	---	---

not active: conversion, rate, and selectivity are similar to the empty reactor
$rate_i$, X_i, S_i: initial rate, conversion, and selectivity at TOS= 5 min
$rate_f$, X_f, S_f: final rate, conversion, and selectivity at TOS= 10 hrs

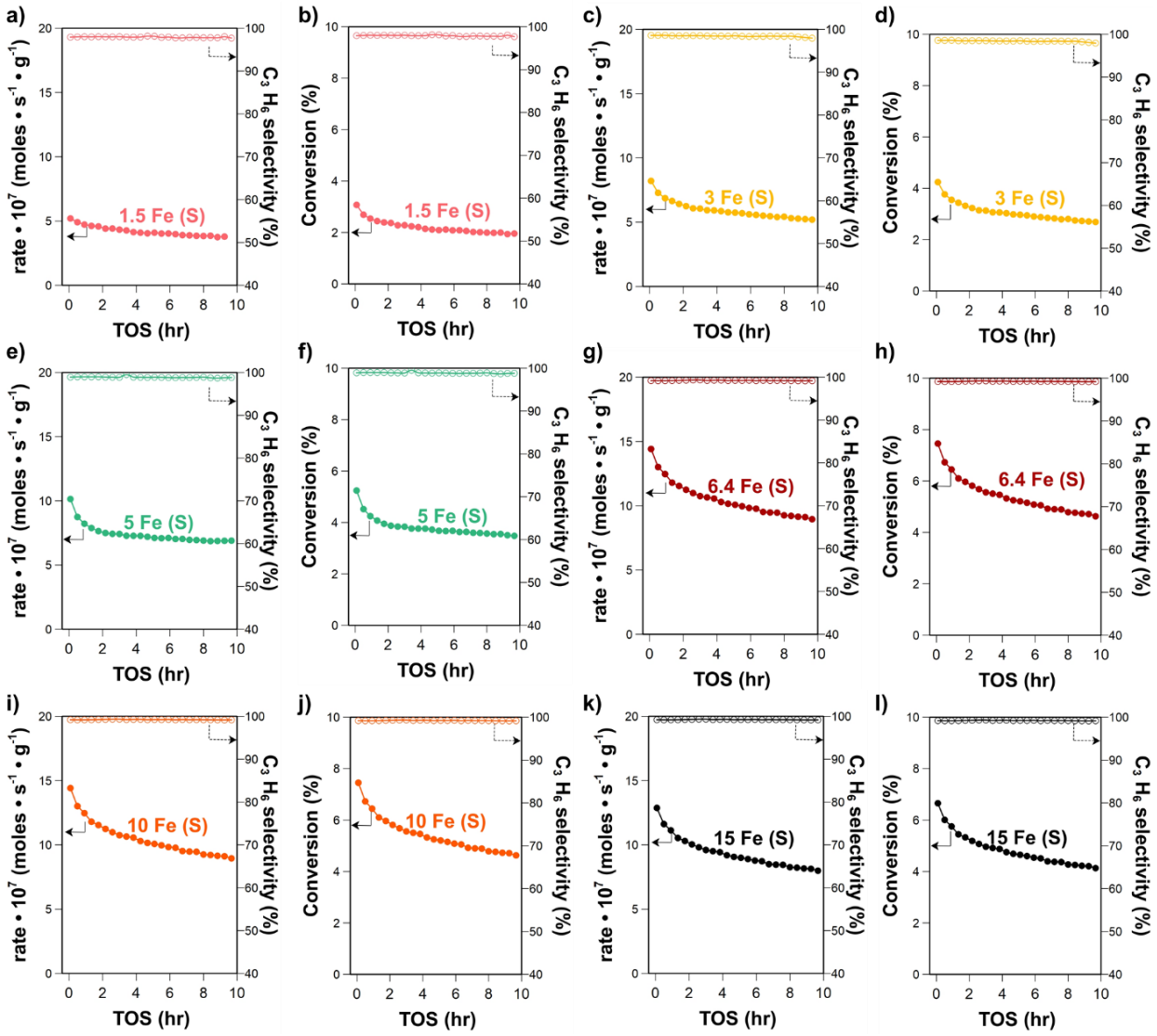

Figure S23. Rate and conversion for different catalysts are reported in **Table S7** and **Figure 7b**. Reaction conditions were as follows: T=560 °C, C_3H_8=1.05%, H_2=1%, and H_2S =0.1% (if present) and 30 mg of catalyst was used. The total volumetric flow rate was 75 ml/min. The catalysts were pretreated in a 1 mol% H_2S stream at 600 °C for 4 hrs. This figure reports the data under differential conditions.

Table S7. Tabulated steady-state reactivity properties of the Fe supported catalysts with different Fe (wt.%) loading. Reaction conditions were as follows: T=560 °C, C_3H_8=1.05%, H_2=1%, and H_2S =0.1% (if present) and 30 mg of catalyst was used. The total volumetric flow rate was 75 ml/min to achieve differential conversion. This table reports the differential conversion data (shown in **Figure 7b**).

Co-feed	**Catalyst**	**S_i (%)**	**$rate_i$** (moles g^{-1} s^{-1}) [**X_i** (%)]	**S_f (%)**	**$rate_f$** (moles g^{-1} s^{-1}) [**X_f** (%)]	**TOF ×10^{-3}** (s^{-1})	**F/I**
$H_2 + H_2S$	Al_2O_3-S	93.3	2.79 ×10^{-7} [1.43]	---	---	---	---
$H_2 + H_2S$	1.5 Fe/Al_2O_3-S	98.0	5.94 ×10^{-7} [3.07]	98.0	3.70 ×10^{-7} [1.92]	2.54	0.63
$H_2 + H_2S$	3 Fe/Al_2O_3-S	98.6	8.14×10^{-7} [4.17]	98.7	5.10 ×10^{-7} [2.5]	2.45	0.63
$H_2 + H_2S$	5 Fe/Al_2O_3-S	98.9	10.1 ×10^{-7} [5.2]	98.8	6.60×10^{-7} [3.45]	2.69	0.66
$H_2 + H_2S$	6.4 Fe/Al_2O_3-S	99.2	14.4 ×10^{-7} [7.45]	99.1	8.95 ×10^{-7} [4.6]	2.94	0.62
$H_2 + H_2S$	10 Fe/Al_2O_3-S	99.2	14.3 ×10^{-7} [7.3]	99.1	9.21 ×10^{-7} [4.7]	2.92	0.64
$H_2 + H_2S$	15 Fe/Al_2O_3-S	99.4	12.7 ×10^{-7} [6.7]	99.3	8.25 ×10^{-7} [4.3]	2.67	0.63

$rate_i$, X_i, S_i: initial rate, conversion, and selectivity at TOS= 5 min

$rate_f$, X_f, S_f: final rate, conversion, and selectivity at TOS= 10 hrs

The slight improvement from 98% (1.5 Fe/Al_2O_3-S) to 99% (6.4 Fe/Al_2O_3-S) in selectivity at higher loading could be due to gradual covering of exposed Al_2O_3 sites.

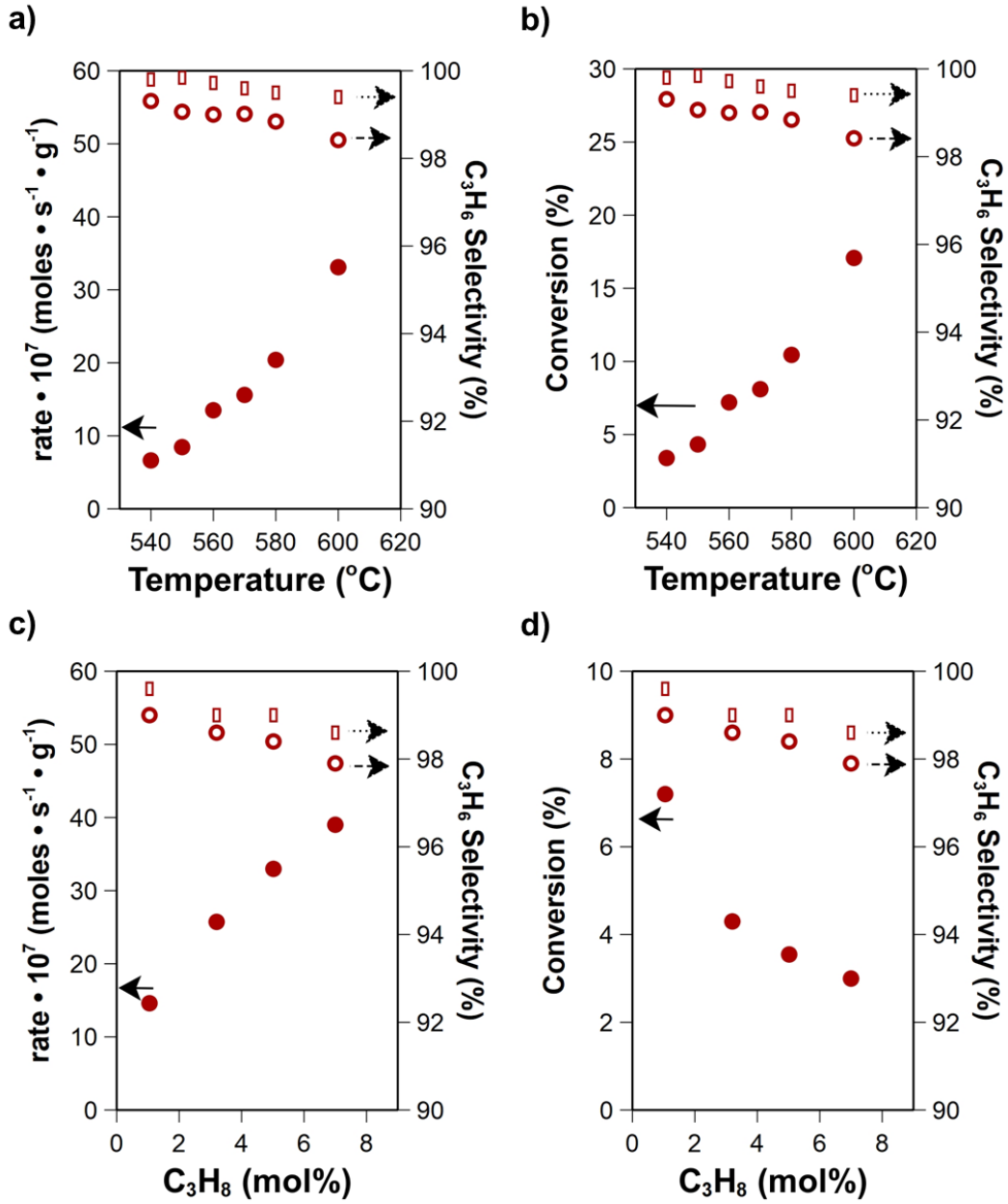

Figure S24. Observed kinetics of propane dehydrogenation reaction on 6.4 Fe/Al_2O_3-S. (a) the effect on the rate and (b) conversion with varying temperature (540−600 °C), with the feed containing 1.05% C_3H_8, 1% H_2, 0.1% H_2S with the balance N_2. Partial pressure dependence of PDH kinetics on (b) propane (varied 1−7 mol %) is also shown. The concentrations of H_2 and H_2S were 1 and 0.1% were fixed, with balance N_2, such that the total flow rate of 75 ml/min was ensured; the temperature was fixed at 560 °C. 30 mg of catalyst was utilized. The catalysts were pretreated in a 1 mol% H_2S stream at 600 °C for 4 hrs. The initial rates at TOS = 5mins are reported in the figure. Solid circles represent reaction rate or conversion, while empty circles represent C_3H_6 selectivity (uncorrected). The empty barverts represents corrected selectivity, i.e., after subtraction of gas-phase contributions determined by running reactor with SiO_2 sand particles.

The thermal conversion was low. The rate of formation of CH_4 and C_2H_4 due to thermal conversion was comparable under differential conditions. However, the amount of CH_4 and C_2H_4 formed in the gas phase was significant and was subtracted to calculate the corrected catalyst selectivity.

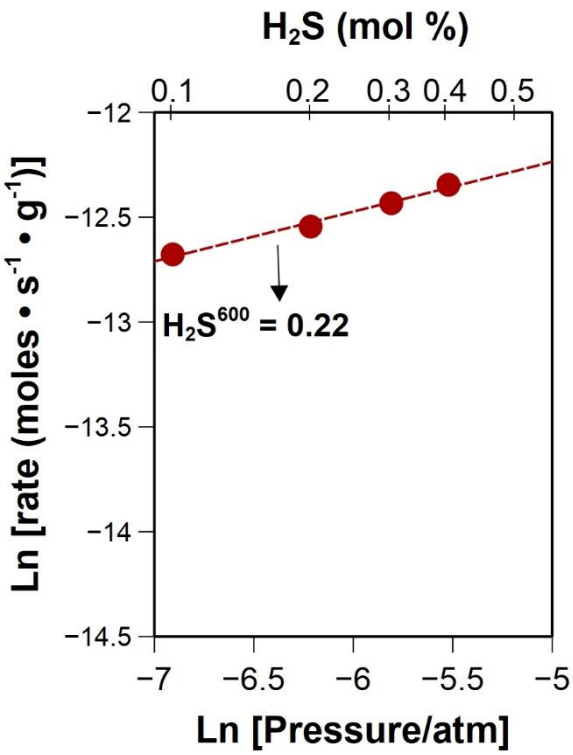

Figure S25. Observed kinetics of propane dehydrogenation reaction on 6.4 Fe/Al_2O_3-S. H_2S (varied 0.1−0.5 mol %) is also shown. The reference concentrations of C_3H_8, H_2 and H_2S were 1.05, 1 and 0.1%, with balance N_2, such that the 30 mg of catalyst and total flow rate of 75 ml/min was ensured; the temperature was fixed at 600 °C. The catalysts were pretreated in a 1 mol% H_2S stream at 600 °C for 4 hrs. The initial rates at TOS = 5mins are reported in the figure. The dashed line is the linear fits to the data.

Table S8. Summary of the catalytic data and reaction conditions of various catalysts .

Catalyst	Temp in °C	Composition (%)	S (%)	X (%)	Rate (mole g^{-1} s^{-1})	TOF (s^{-1})	ref
Al_2O_3-S	560	C_3H_8=1.1, H_2=1	88	20	4.36 $\times 10^{-7}$	---	[12]
Al_2O_3-S	560	C_3H_8 =1.1, H_2=1, H_2S=0.1	94	15.9	3.31 $\times 10^{-7}$	---	[12]
6.4 Fe/Al_2O_3-S	560	C_3H_8 =1.05, H_2=1, H_2S=0.1	99.2	7.5	14.4 $\times 10^{-7}$	2.94 $\times 10^{-3}$	#
6.4 Fe/Al_2O_3-S	600	C_3H_8 =1.05, H_2=1, H_2S=0.1	98.0	17.5	34.1 $\times 10^{-7}$	6.95 $\times 10^{-3}$	#
6.4 Fe/Al_2O_3-S	560	C_3H_8 =7, H_2=1, H_2S=0.1	97.8	3.0	39.0 $\times 10^{-7}$	8.0 $\times 10^{-3}$	#
Pt/Mg(In)(Al)O@ Al_2O_3	600	C_3H_8 =20; H_2=25	99	--	6.70E-05	3.0	[13]
0.50 wt% Pt/Mg(Sn)(Al)O	550	C_3H_8 =29; H_2=14	94	29.4	2.78E-05	0.96	[14]
0.50 wt% Pt/Mg(Sn)(Al)O	600	C_3H_8 =29; H_2=14	87	48.3	4.56E-05	1.46	[14]
Sn-HMS	600	C_3H_8 =99.8	90	39	3.6 $\times 10^{-7}$	3.4 $\times 10^{-3}$	[15]
Sn-DMSN	600	C_3H_8 =100	88	17.3	34 $\times 10^{-7}$	23.9 $\times 10^{-3}$	[16]
30 VO_x-SiO_2	580	C_3H_8 =10	90	65	---	2.5 $\times 10^{-3}$	[17]
(3Fe:P)/Al_2O_3	600	C_3H_8 =5	82.4	14	27.5 $\times 10^{-7}$	5.2 $\times 10^{-3}$	[18]
Co–Al_2O_3–HT	590	C_3H_8 =20; H_2 = 18	96	25	45 $\times 10^{-7}$	---	[19]
5 Si - 5 Co–Al_2O_3	590	C_3H_8 =20; H_2 = 18	90	24	---	---	[20]
5 Si - 5 Co–Al_2O_3	590	C_3H_8 =20; H_2 = 18	90	6	---	23.6 $\times 10^{-3}$	[20]
Ru-P/SiO_2-50	600	C_3H_8 =2.5; H_2 = 2.5	94	26	---	1.9 $\times 10^{-3}$	[21]

# indicates the present work, values of initial selectivity and conversion are reported.

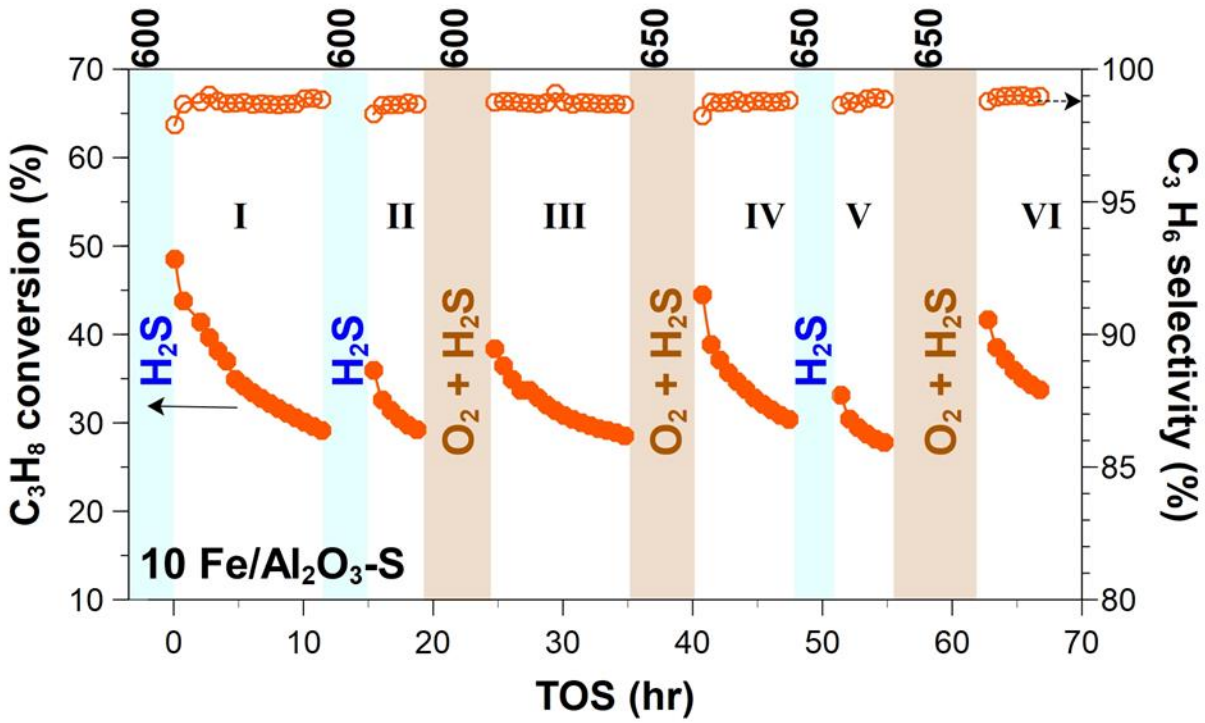

Cycle I & II: H_2S pretreatment for 4 hr at 600 °C
Cycle III: O_2 (2%) for 1 hr followed by H_2S pretreatment for 4 hr at 600 °C
Cycle IV: O_2 (2%) for 2 hr followed by H_2S pretreatment for 4 hr at 650 °C
Cycle V: H_2S pretreatment for 4 hr at 650 °C
Cycle VI: O_2 (2%) for 4 hr followed by H_2S pretreatment for 4 hr at 600 °C

Figure S26. Measured regeneration of 6.4 Fe/Al_2O_3-S by a combination of H_2S or H_2S/O_2 treatments. C_3H_8 conversion and C_3H_6 selectivity for different pretreatments for 10 Fe/Al_2O_3-S. The feed contained 1.1% C_3H_8, 1% H_2, with (0.1%) H_2S co-feed, and the reaction temperature was 560 °C for all cycle. The total volumetric flow rate was 50 ml/min and 200 mg of catalyst was used. Solid octagon represent conversion, while empty octagon represent C_3H_6 selectivity.

References

(1) Yan, W.; Luo, J.; Kouk, Q.-Y.; Zheng, J.; Zhong, Z.; Liu, Y.; Borgna, A. Improving Oxidative Dehydrogenation of 1-Butene to 1,3-Butadiene on Al2O3 by Fe2O3 Using CO2 as Soft Oxidant. *Appl. Catal. A Gen.* **2015**, *508*, 61–67. https://doi.org/https://doi.org/10.1016/j.apcata.2015.10.012.

(2) Ramselaar, W. L. T. M.; Crajé, M. W. J.; Hadders, R. H.; Gerkema, E.; de Beer, V. H. J.; van der Kraan, A. M. Sulfidation of Alumina-Supported Iron and Iron-Molybdenum Oxide Catalysts. *Appl. Catal.* **1990**, *65* (1), 69–84. https://doi.org/https://doi.org/10.1016/S0166-9834(00)81589-4.

(3) Zhong, Z. Y.; Prozorov, T.; Felner, I.; Gedanken, A. Sonochemical Synthesis and Characterization of Iron Oxide Coated on Submicrospherical Alumina: A Direct Observation of Interaction between Iron Oxide and Alumina. *J. Phys. Chem. B* **1999**, *103* (6), 947–956. https://doi.org/10.1021/jp983164z.

(4) Hoffmann, D. P.; Houalla, M.; Proctor, A.; Fay, M. J.; Hercules, D. M. Quantitative Characterization of Fe/Al2O3 Catalysts. Part I: Oxidic Precursors. *Appl. Spectrosc.* **1992**, *46* (2), 208–218. https://doi.org/10.1366/0003702924125618.

(5) Zhou, L.; Enakonda, L. R.; Saih, Y.; Loptain, S.; Gary, D.; Del-Gallo, P.; Basset, J.-M. Catalytic Methane Decomposition over Fe-Al2O3. *ChemSusChem* **2016**, *9* (11), 1243–1248. https://doi.org/10.1002/cssc.201600310.

(6) Zhao, W.; Zheng, X.; Liang, S.; Zheng, X.; Shen, L.; Liu, F.; Cao, Y.; Wei, Z.; Jiang, L. Fe-Doped γ-Al2O3 Porous Hollow Microspheres for Enhanced Oxidative Desulfurization: Facile Fabrication and Reaction Mechanism. *Green Chem.* **2018**, *20* (20), 4645–4654. https://doi.org/10.1039/C8GC02184H.

(7) Colaianni, M. L.; Chen, P. J.; Yates, J. T. Spectroscopic Studies of the Thermal Modification of the Fe/Al2O3 Interface. *Surf. Sci.* **1990**, *238* (1), 13–24. https://doi.org/https://doi.org/10.1016/0039-6028(90)90061-C.

(8) Vuurman, M. A.; Wachs, I. E. Raman Spectroscopy of V2O5, MoO3, Fe2O3, MoO3-V2O5, and Fe2O3-V2O5 Supported on Alumina Catalysts: Influence of Coverage and Dehydration. *J. Mol. Catal.* **1992**, *77* (1), 29–39. https://doi.org/https://doi.org/10.1016/0304-5102(92)80182-G.

(9) Jehng, J.-M.; Wachs, I. E.; Clark, F. T.; Springman, M. C. Raman Characterization of Alumina Supported Mo-V-Fe Catalysts: Influence of Calcination Temperature. *J. Mol. Catal.* **1993**, *81* (1), 63–75. https://doi.org/https://doi.org/10.1016/0304-5102(93)80023-N.

(10) D'Ippolito, V.; Andreozzi, G. B.; Bersani, D.; Lottici, P. P. Raman Fingerprint of Chromate, Aluminate and Ferrite Spinels. *J. Raman Spectrosc.* **2015**, *46* (12), 1255–1264. https://doi.org/https://doi.org/10.1002/jrs.4764.

(11) Mansour, H.; Letifi, H.; Bargougui, R.; De Almeida-Didry, S.; Negulescu, B.; Autret-Lambert, C.; Gadri, A.; Ammar, S. Structural, Optical, Magnetic and Electrical Properties of Hematite (α-Fe2O3) Nanoparticles Synthesized by Two Methods: Polyol and Precipitation. *Appl. Phys. A* **2017**, *123* (12), 787. https://doi.org/10.1007/s00339-017-1408-1.

(12) Sharma, L.; Jiang, X.; Wu, Z.; Baltrus, J.; Rangarajan, S.; Baltrusaitis, J. Elucidating the Origin of Selective Dehydrogenation of Propane on γ-Alumina under H2S Treatment and Co-Feed. *J. Catal.* **2021**, *394*, 142–156. https://doi.org/https://doi.org/10.1016/j.jcat.2020.12.018.

(13) Sun, P.; Siddiqi, G.; Vining, W. C.; Chi, M.; Bell, A. T. Novel Pt/Mg(In)(Al)O Catalysts

for Ethane and Propane Dehydrogenation. *J. Catal.* **2011**, *282* (1), 165–174. https://doi.org/https://doi.org/10.1016/j.jcat.2011.06.008.

(14) Zhu, Y.; An, Z.; Song, H.; Xiang, X.; Yan, W.; He, J. Lattice-Confined Sn (IV/II) Stabilizing Raft-Like Pt Clusters: High Selectivity and Durability in Propane Dehydrogenation. *ACS Catal.* **2017**, *7* (10), 6973–6978. https://doi.org/10.1021/acscatal.7b02264.

(15) Wang, G.; Zhang, H.; Zhu, Q.; Zhu, X.; Li, X.; Wang, H.; Li, C.; Shan, H. Sn-Containing Hexagonal Mesoporous Silica (HMS) for Catalytic Dehydrogenation of Propane: An Efficient Strategy to Enhance Stability. *J. Catal.* **2017**, *351*, 90–94. https://doi.org/https://doi.org/10.1016/j.jcat.2017.04.018.

(16) Liu, Q.; Luo, M.; Zhao, Z.; Zhao, Q. K-Modified Sn-Containing Dendritic Mesoporous Silica Nanoparticles with Tunable Size and SnOx-Silica Interaction for the Dehydrogenation of Propane to Propylene. *Chem. Eng. J.* **2020**, *380*, 122423. https://doi.org/https://doi.org/10.1016/j.cej.2019.122423.

(17) Hu, P.; Lang, W.-Z.; Yan, X.; Chu, L.-F.; Guo, Y.-J. Influence of Gelation and Calcination Temperature on the Structure-Performance of Porous VOX-SiO2 Solids in Non-Oxidative Propane Dehydrogenation. *J. Catal.* **2018**, *358*, 108–117. https://doi.org/https://doi.org/10.1016/j.jcat.2017.12.004.

(18) Tan, S.; Hu, B.; Kim, W.-G.; Pang, S. H.; Moore, J. S.; Liu, Y.; Dixit, R. S.; Pendergast, J. G.; Sholl, D. S.; Nair, S.; Jones, C. W. Propane Dehydrogenation over Alumina-Supported Iron/Phosphorus Catalysts: Structural Evolution of Iron Species Leading to High Activity and Propylene Selectivity. *ACS Catal.* **2016**, *6* (9), 5673–5683. https://doi.org/10.1021/acscatal.6b01286.

(19) Dai, Y.; Gu, J.; Tian, S.; Wu, Y.; Chen, J.; Li, F.; Du, Y.; Peng, L.; Ding, W.; Yang, Y. γ-Al2O3 Sheet-Stabilized Isolate Co2+ for Catalytic Propane Dehydrogenation. *J. Catal.* **2020**, *381*, 482–492. https://doi.org/https://doi.org/10.1016/j.jcat.2019.11.026.

(20) Dai, Y.; Wu, Y.; Dai, H.; Gao, X.; Tian, S.; Gu, J.; Yi, X.; Zheng, A.; Yang, Y. Effect of Coking and Propylene Adsorption on Enhanced Stability for Co2+-Catalyzed Propane Dehydrogenation. *J. Catal.* **2021**, *395*, 105–116. https://doi.org/https://doi.org/10.1016/j.jcat.2020.12.021.

(21) Ma, R.; Yang, T.; Gao, J.; Kou, J.; Chen, J. Z.; He, Y.; Miller, J. T.; Li, D. Composition Tuning of Ru-Based Phosphide for Enhanced Propane Selective Dehydrogenation. *ACS Catal.* **2020**, *10* (17), 10243–10252. https://doi.org/10.1021/acscatal.0c01667.